Deep neural network for pixel-level electromagnetic particle identification in the MicroBooNE liquid argon time projection chamber

C. Adams,[10] M. Alrashed,[12] R. An,[11] J. Anthony,[3] J. Asaadi,[28] A. Ashkenazi,[16] M. Auger,[1] S. Balasubramanian,[32] B. Baller,[9] C. Barnes,[17] G. Barr,[20] M. Bass,[2] F. Bay,[29] A. Bhat,[25] K. Bhattacharya,[21] M. Bishai,[2] A. Blake,[13] T. Bolton,[12] L. Camilleri,[7] D. Caratelli,[9] I. Caro Terrazas,[6] R. Carr,[16] R. Castillo Fernandez,[9] F. Cavanna,[9] G. Cerati,[9] Y. Chen,[1] E. Church,[21] D. Cianci,[7] E. O. Cohen,[26] G. H. Collin,[16] J. M. Conrad,[16] M. Convery,[24] L. Cooper-Troendle,[32] J. I. Crespo-Anadón,[7] M. Del Tutto,[20] D. Devitt,[13] A. Diaz,[16] K. Duffy,[9] S. Dytman,[22] B. Eberly,[24,8] A. Ereditato,[1] L. Escudero Sanchez,[3] J. Esquivel,[25] J. J. Evans,[15] A. A. Fadeeva,[7] R. S. Fitzpatrick,[17] B. T. Fleming,[32] D. Franco,[32] A. P. Furmanski,[15] D. Garcia-Gamez,[15] V. Genty,[7] D. Goeldi,[1] S. Gollapinni,[27] O. Goodwin,[15] E. Gramellini,[32] H. Greenlee,[9] R. Grosso,[5] R. Guenette,[10] P. Guzowski,[15] A. Hackenburg,[32] P. Hamilton,[25] O. Hen,[16] J. Hewes,[15] C. Hill,[15] G. A. Horton-Smith,[12] A. Hourlier,[16] E.-C. Huang,[14] C. James,[9] J. Jan de Vries,[3] X. Ji,[2] L. Jiang,[22] R. A. Johnson,[5] J. Joshi,[2] H. Jostlein,[9] Y.-J. Jwa,[7] G. Karagiorgi,[7] W. Ketchum,[9] B. Kirby,[2] M. Kirby,[9] T. Kobilarcik,[9] I. Kreslo,[1] I. Lepetic,[11] Y. Li,[2] A. Lister,[13] B. R. Littlejohn,[11] S. Lockwitz,[9] D. Lorca,[1] W. C. Louis,[14] M. Luethi,[1] B. Lundberg,[9] X. Luo,[32] A. Marchionni,[9] S. Marcocci,[9] C. Mariani,[31] J. Marshall,[3] J. Martin-Albo,[10] D. A. Martinez Caicedo,[11] A. Mastbaum,[4] V. Meddage,[12] T. Mettler,[1] K. Mistry,[15] A. Mogan,[27] J. Moon,[16] M. Mooney,[6] C. D. Moore,[9] J. Mousseau,[17] M. Murphy,[31] R. Murrells,[15] D. Naples,[22] P. Nienaber,[23] J. Nowak,[13] O. Palamara,[9] V. Pandey,[31] V. Paolone,[22] A. Papadopoulou,[16] V. Papavassiliou,[18] S. F. Pate,[18] Z. Pavlovic,[9] E. Piasetzky,[26] D. Porzio,[15] G. Pulliam,[25] X. Qian,[2] J. L. Raaf,[9] A. Rafique,[12] L. Ren,[18] L. Rochester,[24] M. Ross-Lonergan,[7] C. Rudolf von Rohr,[1] B. Russell,[32] G. Scanavini,[32] D. W. Schmitz,[4] A. Schukraft,[9] W. Seligman,[7] M. H. Shaevitz,[7] R. Sharankova,[30] J. Sinclair,[1] A. Smith,[3] E. L. Snider,[9] M. Soderberg,[25] S. Söldner-Rembold,[15] S. R. Soleti,[20,10] P. Spentzouris,[9] J. Spitz,[17] J. St. John,[9] T. Strauss,[9] K. Sutton,[7] S. Sword-Fehlberg,[18] A. M. Szelc,[15] N. Tagg,[19] W. Tang,[27] K. Terao,[24] M. Thomson,[3] R. T. Thornton,[14] M. Toups,[9] Y.-T. Tsai,[24] S. Tufanli,[32] T. Usher,[24] W. Van De Pontseele,[20,10] R. G. Van de Water,[14] B. Viren,[2] M. Weber,[1] H. Wei,[2] D. A. Wickremasinghe,[22] K. Wierman,[21] Z. Williams,[28] S. Wolbers,[9] T. Wongjirad,[30] K. Woodruff,[18] T. Yang,[9] G. Yarbrough,[27] L. E. Yates,[16] G. P. Zeller,[9] J. Zennamo,[9] and C. Zhang[2]

(MicroBooNE Collaboration)[*]

[1]*Universität Bern, Bern CH-3012, Switzerland*
[2]*Brookhaven National Laboratory (BNL), Upton, New York 11973, USA*
[3]*University of Cambridge, Cambridge CB3 0HE, United Kingdom*
[4]*University of Chicago, Chicago, Illinois 60637, USA*
[5]*University of Cincinnati, Cincinnati, Ohio 45221, USA*
[6]*Colorado State University, Fort Collins, Colorado 80523, USA*
[7]*Columbia University, New York, New York 10027, USA*
[8]*Davidson College, Davidson, North Carolina 28035, USA*
[9]*Fermi National Accelerator Laboratory (FNAL), Batavia, Illinois 60510, USA*
[10]*Harvard University, Cambridge, Massachusetts 02138, USA*
[11]*Illinois Institute of Technology (IIT), Chicago, Illinois 60616, USA*
[12]*Kansas State University (KSU), Manhattan, Kansas 66506, USA*
[13]*Lancaster University, Lancaster LA1 4YW, United Kingdom*
[14]*Los Alamos National Laboratory (LANL), Los Alamos, New Mexico 87545, USA*
[15]*The University of Manchester, Manchester M13 9PL, United Kingdom*
[16]*Massachusetts Institute of Technology (MIT), Cambridge, Massachusetts 02139, USA*
[17]*University of Michigan, Ann Arbor, Michigan 48109, USA*
[18]*New Mexico State University (NMSU), Las Cruces, New Mexico 88003, USA*
[19]*Otterbein University, Westerville, Ohio 43081, USA*
[20]*University of Oxford, Oxford OX1 3RH, United Kingdom*
[21]*Pacific Northwest National Laboratory (PNNL), Richland, Washington 99352, USA*
[22]*University of Pittsburgh, Pittsburgh, Pennsylvania 15260, USA*
[23]*Saint Mary's University of Minnesota, Winona, Minnesota 55987, USA*
[24]*SLAC National Accelerator Laboratory, Menlo Park, California 94025, USA*
[25]*Syracuse University, Syracuse, New York 13244, USA*
[26]*Tel Aviv University, Tel Aviv, Israel, 69978*
[27]*University of Tennessee, Knoxville, Tennessee 37996, USA*

[28]*University of Texas, Arlington, Texas 76019, USA*
[29]*TUBITAK Space Technologies Research Institute, METU Campus, TR-06800, Ankara, Turkey*
[30]*Tufts University, Medford, Massachusetts 02155, USA*
[31]*Center for Neutrino Physics, Virginia Tech, Blacksburg, Virginia 24061, USA*
[32]*Yale University, New Haven, Connecticut 06520, USA*

We have developed a convolutional neural network that can make a pixel-level prediction of objects in image data recorded by a liquid argon time projection chamber (LArTPC) for the first time. We describe the network design, training techniques, and software tools developed to train this network. The goal of this work is to develop a complete deep neural network based data reconstruction chain for the MicroBooNE detector. We show the first demonstration of a network's validity on real LArTPC data using MicroBooNE collection plane images. The demonstration is performed for stopping muon and a ν_μ charged-current neutral pion data samples.

I. INTRODUCTION

Liquid argon time projection chambers (LArTPCs) are capable of producing high-resolution images of particle interactions. This is one of the main reasons LArTPCs are the technology of choice for several current and future neutrino research programs including the Short Baseline Program (SBN) [1] and Deep Underground Neutrino Experiment (DUNE) [2]. The MicroBooNE experiment [3], as a part of the SBN program, studies the ν_e-like low-energy (LE) event excess observed by the MiniBooNE Collaboration [4] using a LArTPC detector and the on-axis Booster Neutrino Beamline (BNB) [5] at Fermilab as the ν_μ source.

A LArTPC consists of a homogeneous volume of liquid argon bounded by a cathode plane and an anode plane. When a charged particle traverses the sensitive region, ionization electrons and scintillation light are produced along its trajectory. The scintillation light is detected within several nanoseconds by an array of photomultiplier tubes, providing a timing measurement. Ionization electrons take a few milliseconds to drift toward the anode under the applied electric field and are detected by the anode plane, which is equipped with a set of wire planes and charge-sensitive readout circuits. The spatial separation within the wires on the anode plane determines the spatial resolution of the recorded two-dimensional (2D) projection images. The speed of drift electrons along with their longitudinal diffusion, as well as the electronics response and the sampling frequency

of the signal waveform determine the spatial resolution along the drift direction.

While the detector is able to capture many of the fine details that will be useful for physics analysis, parsing these details using automated reconstruction tools is still a technical challenge. One particular challenge is the discrimination between electromagnetic (EM) particles, namely e^-, e^+, and photons, and other particle types. EM particles above the critical energy ($\approx$33 MeV in argon) initiate an electromagnetic cascade of particles and develop a unique topology that consists of a collection of branching features. Identifying this topology is a simple form of particle identification, and is key information that can be used to discriminate between ν_e and ν_μ interactions, as shown in Fig. 1. For EM particles below the critical energy, other unique features are available. One example is low-energy electrons (δ rays) knocked off from argon atoms by a muon traversing the detector. These add multiple short *branches* to a muon trajectory. Separating them from a muon helps to identify the trunk of a muon trajectory. Another example is a Michel electron trajectory with low-energy deposition per unit length (dE/dx) from the decay of a stopping muon. That trajectory typically exhibits a
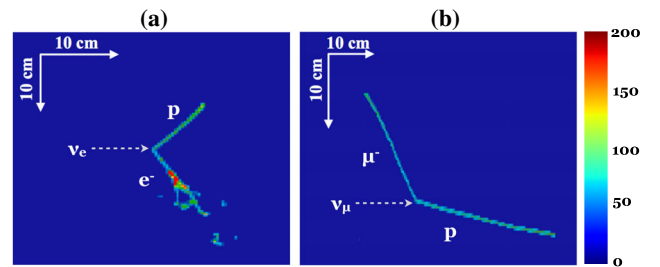
FIG. 1. Two examples of ν_e (a) and ν_μ (b) events simulated in the MicroBooNE detector. The pixel color represents the amount of energy deposited per pixel in the 2D projection image. The pattern of ionization differs significantly between ν_e and ν_μ.
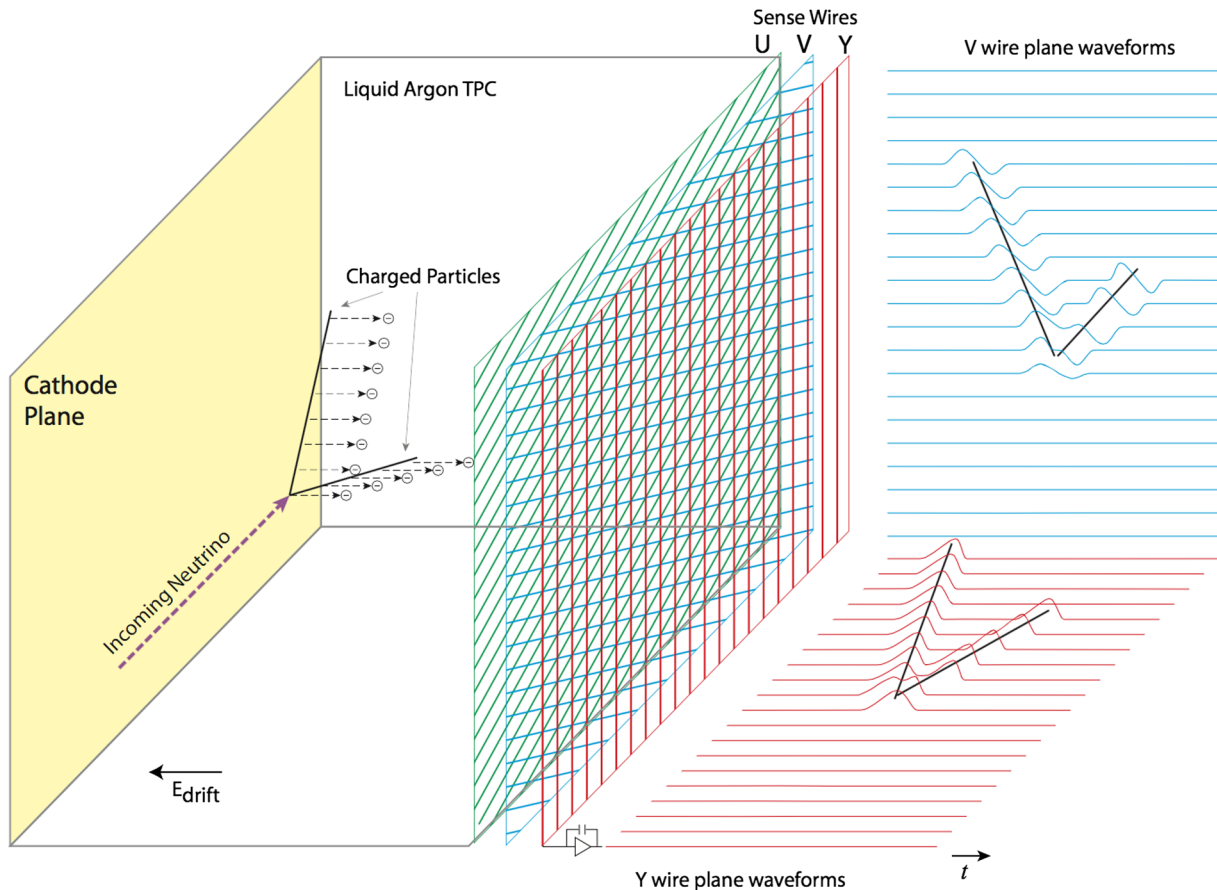
FIG. 2.   The MicroBooNE detector schematics showing three wire planes and example 2D projections of V and Y plane waveforms.

pattern of increasing dE/dx due to an increase in ionization energy loss as it comes to rest. Identifying and cleanly separating energy depositions from Michel electrons in the muon decay allows one to reconstruct the Michel spectrum with high accuracy. This sample proves to be a valuable energy calibration source.

In this paper, we demonstrate that EM particles can be discriminated from other particles at the pixel level in an image using a class of machine learning algorithms known as convolutional neural networks (CNNs). We refer to EM particles as *shower* and the others as *track* particles in the rest of the paper. Our method uses noise-filtered, signal shape deconvolved waveforms [6] from the charge-collection plane organized in 2D image format prior to a pixel clustering analysis. Having a prediction of each pixel as track or shower type prior to a pixel clustering reconstruction stage simplifies the downstream pattern-recognition algorithms and reduces the need for iterative reconstruction processes. We use a class of CNNs called *semantic segmentation networks* (SSNets) to classify each pixel of an image into a predefined set of semantics including a track, a shower, and a background pixel.

This work was performed as a step towards the development of a complete LArTPC event reconstruction and analysis chain using deep neural networks. It is an extension of an earlier study in which we demonstrated the use of image classification and object detection techniques with CNNs for LArTPC data analysis [7]. Examples of the application of CNNs to neutrino data analysis in other detectors can be found in Refs. [8–12]. The new contributions in this work include

(i)   First demonstration of a pixel-level object prediction for LArTPC event reconstruction using a deep neural network.

(ii)   First demonstration of a deep neural network on real LArTPC detector data.

(iii)   Software tools and algorithms capable of generating a pixel-level *label* (i.e., semantics) from LArSoft [13] data for supervised training and analysis of real detector data.

The software is open source and accessible at Ref. [14].

The deep neural network described here is currently employed in the data reconstruction chain for the deep-learning based analysis of the MiniBooNE low-energy excess by MicroBooNE. The analysis goal is to locate a neutrino interaction vertex and identify the interaction type as being ν_e or ν_μ for low-energy neutrinos (≈ 200 to 600 MeV). Having track/shower separation information is crucial for vertex reconstruction and particle clustering algorithms.

High rate environments, as in LArTPCs like the Short Baseline Near Detector and the DUNE near detector, both to be built in the not-too-distant future at Fermilab, will benefit from sophisticated computer vision techniques. Such techniques, including pixel labeling as provided by the semantic segmentation approach described here, will be very useful to untangle neutrino-induced tracks and showers.

II. MICROBOONE DETECTOR AND PARTICLE IMAGES

The MicroBooNE LArTPC contains 85 metric tons of liquid argon in the active region, which is defined by a rectangular shape with the dimensions 10.36 m in length, 2.32 m in height, and 2.56 m in width along the drift direction [3], as shown in Fig. 2. The anode consists of three planes of parallel wires. The first and second planes contain 2,400 wires with orientations of $+60$ and -60 degrees from the vertical, respectively. Ionization electrons produce bipolar signals on the two *induction* planes as they pass through them. The third is called the *collection* plane and consists of 3,456 vertical wires. Wires on the third plane are held at a positive potential and collect ionization electrons. Wires are separated by 3 mm pitch in all planes, and signal waveforms are digitized at a 2 MHz sampling rate and recorded for a duration of 4.8 ms in each event. Combined wire waveforms, aligned by the digitization

time, form 2D projected images of a three-dimensional (3D) particle trajectory from a different projection angle. The digitization time runs along the vertical axis and the wires run along the horizontal axis in event displays shown in this paper (e.g., Fig. 1).

In this paper we focus on the analysis of image data recorded by the collection plane, which has a size of 3,456 by 9,600 pixels. The spatial resolution of an image along the wire axis is 3 mm per pixel. For the analysis, evebry 6 samples of a digitized waveform are summed together, corresponding to an approximate spatial resolution along the time axis of 3.3 mm. The resulting image dimension is 3,456 by 1,600 pixels.

III. U-RESNET: TRACK/SHOWER PIXEL-LEVEL SEPARATION NETWORK

In this study we use U-ResNet, a hybrid of the U-Net [15] and residual network [16] (ResNet) design pattern. This is a natural approach for semantic segmentation and has been independently explored in other research domains [17,18]. U-ResNet takes a single-channel 512 by 512 pixel image as input and outputs an image of the same spatial dimension with 3 channels per pixel encoding a probability from multinomial logistic regression, or *softmax*, for a pixel being a background, track, or shower type. We use U-Net as the base SSNet architecture design because of its excellent performance in biomedical images [15] which resemble
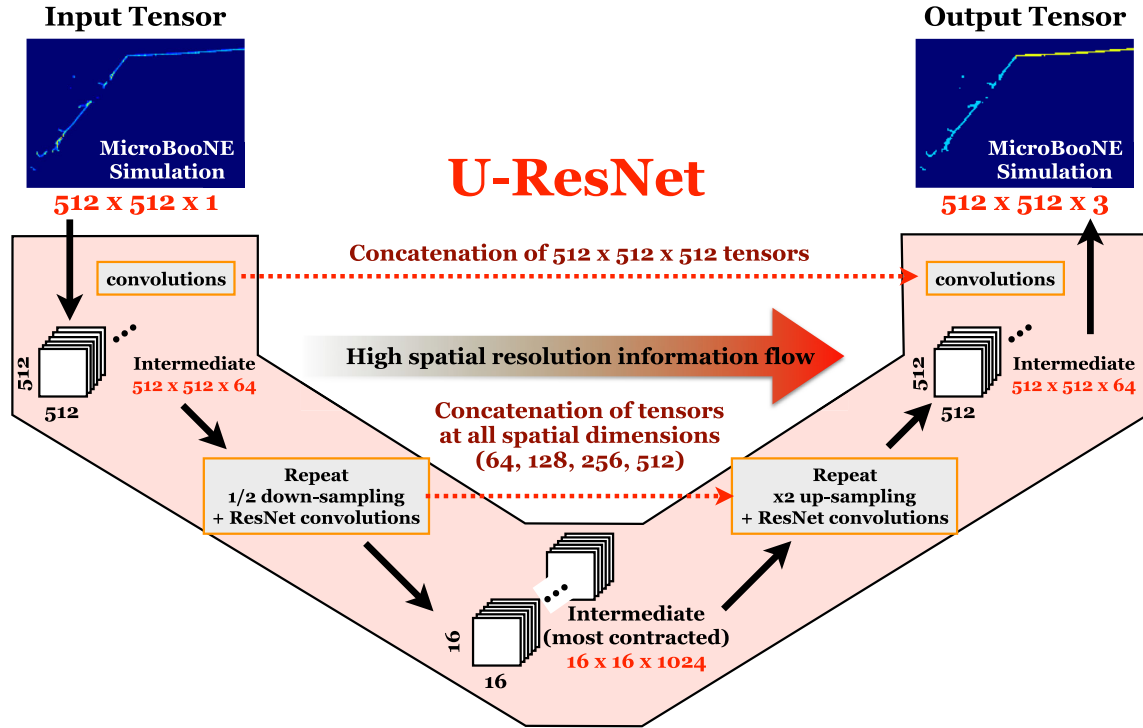

FIG. 3. U-ResNet architecture diagram. Black arrows describe the direction of tensor data flow. Red arrows indicate concatenation operations to combine the output of convolution layers from the encoding path to the decoding path. The final output has the same spatial dimension as the input with a depth of three, representing the background, track and shower probability of each pixel.

those from LArTPCs where information density is sparse. We replace the convolution layers in the original U-Net with ResNet modules. ResNet is a generic CNN design pattern that was invented at the same time as U-Net and enables the training of deep CNNs. In our implementation, each ResNet module consists of two convolution layers of 3-by-3 kernel size, where each convolution layer is followed by a batch normalization operation [19] and a rectified-linear unit activation function. The schematic U-ResNet design is shown in Fig. 3.

The U-ResNet architecture can be interpreted in two separate sections. The first half of the network takes an input image, a data tensor with a dimension of (512,512,1), and repeatedly applies convolution and down-sampling operations. At the end of the first section, the data tensor has a dimension of (16,16,1024). The goal of this section of the network is to learn a nonlinear, hierarchical representation of image features at different scales. Since feature information is encoded in a low spatial resolution tensor at the end of this section of the network, it is referred to as an *encoding path*.

The second half of the U-ResNet takes the output of an encoding path, a tensor with a dimension of (16,16,1024), and repeatedly applies an up-sampling and convolution operation. An up sampling is performed by an operation called *convolution transpose* which is an interpolation filter that expands the spatial dimension of a tensor by a factor of 2. By using neurons to incorporate the interpolation operations, the U-ResNet architecture introduces a *learnable* interpolation filter optimized for assigning object classification to the pixels. This section of the network does essentially the opposite of the encoding path, hence it is called a *decoding path*.

An important and unique design pattern of U-Net is an additional path to allow the flow of information between the encoding path and the decoding path. This mitigates the loss of spatial resolution information in the encoding path where down sampling is performed. The idea and method employed in U-Net is simple and effective; in the decoding path where high spatial resolution needs to be recovered, we concatenate the data tensors from the encoding path where the spatial dimension matches. In the encoding path, data tensors hold the best possible spatial resolution at each spatial resolution prior to the down-sampling operations. Thus a simple concatenation allows information about spatial resolutions to flow into the decoding path, allowing U-Net to perform a high-precision image segmentation.

IV. TRAINING U-RESNET

We train U-ResNet via a supervised learning method that uses simulated particle interaction images. All simulation processes in this study are done using software stacks that can be found in Refs. [13,20]. In this section we describe techniques employed for the training and optimization methods.

A. Transfer learning

We exploit a *transfer learning* technique by first training the first-half of U-ResNet for an image classification task using the identical data set from our previous publication [7]. This data set contains single particle images which could be e^-, photon, muon, π^- or proton. The network's weights trained to discriminate between different particle images provide a natural initial state to perform a pixel-level track/shower separation. When we subsequently train the whole U-ResNet with pretrained weights, we let all network parameters be trained and fine-tuned.

B. Class/pixel-wise loss weighting

Training of the U-ResNet is a process of minimizing the loss, a measure of an error made by the network, over many iterations. The loss is computed by summing over a pixel-wise multinomial logistic loss in each image, and then averaging over all images in a batch of images. This definition of loss presents a challenge to training U-ResNet for LArTPC images where the fraction of pixels that are background is 99% or more, hence dominating the total loss. In order to mitigate this challenge, the authors of the original U-Net paper introduced a class-wise loss weighting factor [15] which is a reciprocal for the number of pixels that belong to each class in an image.

In this study, we introduce a pixel-wise loss (PL) weighting factor that is multiplied by a pixel's loss contribution to the total loss of an image. PL weighting enables the network's training to focus on challenging parts of an image by up weighting a pixel loss in the corresponding regions. For the calculation of PL weighting factors, we define four categories of pixels with the last category separated into particle type instances. The first category contains background (i.e., zero) pixels that surround nonbackground (i.e., nonzero) pixels within 2 pixels. The second category is the rest of background pixels in the image that do not belong to the first category. The third category represents nonzero pixels within 4 pixels of the generated event vertex. Finally, the fourth category is defined for each particle instance and includes nonzero pixels that belong to a particle. Therefore the total number of categories may vary from one event to another. A PL weighting factor is computed per category. It is the reciprocal of the number of pixels belonging to each category. A category with fewer pixel counts represents a rare feature in an image data, and is assigned a higher weighting factor. Figure 4 shows how pixels are grouped into the four categories.

C. Optimization

We use the RMSProp [21] with an initial learning rate of 0.0003 to optimize the U-ResNet. The weights are updated after processing every batch of 60 images. The training process is monitored using the Incorrectly Classified Pixel Fraction (ICPF) metric. Unlike the loss
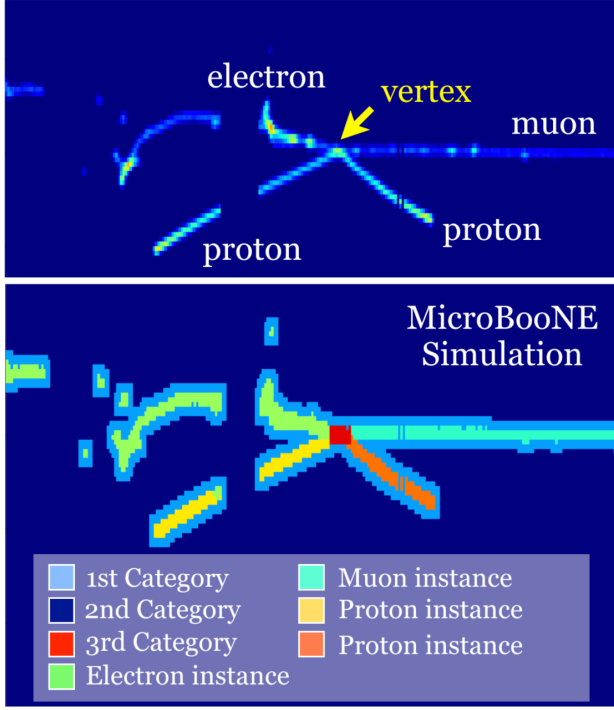
FIG. 4. Top: an example image from the training set in which two protons, one electron, and one muon are produced. The gaps along the trajectory of an electron and proton on the left are due to unresponsive wires [6] in the detector. Bottom: the event from the top image that shows PL weighting categories indicated in different colors.
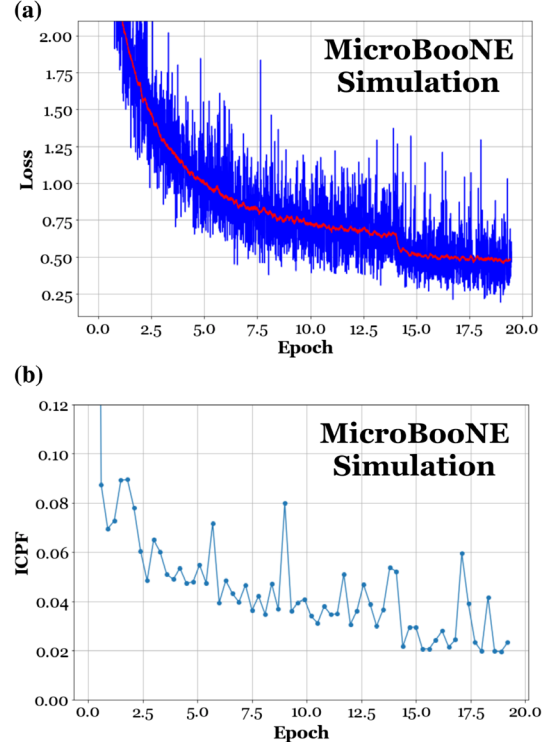

FIG. 5. (a) The training loss value as a function of training time using the validation sample. The red line shows the average at a given Epoch computed using 200 the neighboring Epoch points. (b) ICPF for the same sample. The sudden drop in both figures at Epoch 14 is due to lowering of the learning rate by a factor of 10.

function, this metric does not incorporate the PL weighting factor described above, but instead treats all pixels equally. Figure 5 shows the loss and the average values of ICPF computed over validation samples as a function of epoch during the training. Epoch is a measure of time, and one epoch corresponds to the time it takes to consume the same number of images as the whole training sample. The learning rate is lowered by an order of magnitude at epoch 14 as shown in Fig. 5. We determine the best performing network parameters based on the lowest ICPF value on the *validation set* which is generated independently from the data set used for training under the same simulation configuration. The performance of the network is then quantified using the *test set*, which is yet another independent sample generated with the same simulation configuration. Using the trained network, we find an average ICPF value of 1.9% using all events in the test set. A limited set of variations to the network and training methods were also tested (for example, omitting transfer learning or using a different filter size or loss definition), but these all gave worse or comparable performance.

The U-ResNet and this training scheme is implemented using CAFFE [22], customized to employ the PL weighting scheme [14]. We trained our network using NVIDIA TitanX [23] GPUs with 12 GB memory.

V. DATA SAMPLES FOR TRAINING AND VALIDATION

A. Training sample preparation

We prepare training samples using a custom event generator called MultiPartVertex (MPV), available in the MicroBooNE software repository, UBOONECODE [24]. MPV can be configured to randomly generate a single 3D point in a detector with the emission of multiple charged particles. Any random process employed by MPV is a uniform distribution within the specified range in the configuration. The multiplicity and type of particles to be generated are configurable parameters as outlined below. Restrictions and ranges for the generation are presented in the following two paragraphs.

For 80% of the sample, the MPV is configured to generate events with a random total particle multiplicity between one and four. One of the generated particles must be a light lepton (e^- or μ^-) with kinetic energy ranging from 50 to 1000 MeV. The direction of each particle is chosen from an isotropic distribution. For the other generated particles, the MPV is configured to randomly assign their types to a photon, charged pion, proton, or another lepton (e^- or μ^-). We also set the maximum multiplicity for leptons and protons to be three and photons and charged pions to be two. There is no strong motivation

for this configuration. In fact we demonstrate later in this paper that the network works well on neutrino candidate events with a shower particle from real detector data with multiplicity five.

The remaining 20% of images are generated with a different configuration. The total multiplicity is set randomly between one and four particles but there is no restriction to include at least one light lepton. Instead, particle types are set randomly between showers (e^- and photon) and tracks (μ^-, charged pion, and proton). For each particle type, the maximum multiplicity is set to two. The ranges for the randomly assigned momentum are specified as 30 to 100 MeV/c for e^- and photon, 85 to 175 MeV/c for μ^-, 95 to 195 MeV/c for charged pion, and 300 to 450 MeV/c for proton. The distribution of particle directions is isotropic. This 20% fraction is chosen to have a particular focus on the low-energy region where classification of particle types becomes difficult. The motivation for this is to enhance the networks performance in this energy region. We generate 140 000 images, randomly selecting 100 000 for training, 20 000 for validation, and 20 000 images for testing the network's performance, with no image in more than one set.

After the particle generation stage, the training sample is run through the detector simulation and waveform processing scheme of the experiment. The procedure is similar to that of our previous study [7] but with an updated version of LArSoft [13] and UBOONECODE [24]. The latter software contains important updates including a data-driven detector noise model [6], noise filtering algorithms, and data-driven TPC charge signal deconvolution kernels [25,26]. These improvements aim to reduce the potential discrepancies between data and simulation samples. Hence, these improvements are important for the U-ResNet trained purely on simulation to work effectively on real detector data. Further suppression of the discrepancy between data and simulation for noise with low amplitude is accomplished by setting the pixel value to zero for pixels with amplitude below 10. Finally, we crop the 512 by 512 pixel image from the whole collection plane image which has the original size of 3,456 by 1,600 pixels. These images span an approximate projected area of 1.5 m × 1.5 m and are therefore large compared to the scale (such as the liquid argon radiation length) of features relevant for track/shower pixel labelling. The cropping algorithm (CRA) defines an axis-aligned 3D rectangular volume within the detector of a configurable size that contains a set of 3D points, called constraint points. The location of the 3D box is set by the algorithm under two conditions. First, the defined box must contain all given 3D constraint points. Second, while satisfying the first condition, a range is defined that maximizes the number of nonzero 2D pixels included in the projection of the rectangular box in the collection plane. By satisfying these two conditions, the box location is allowed to float freely. We use the 3D interaction vertex as the constraint point in this study. The resulting 512 by 512 pixel images contain the interaction point location for each event and the maximum number of nonzero pixels in the projection.

B. Benchmark simulation samples

Separately from the testing set, we generate five additional simulation samples to benchmark the performance of U-ResNet. These simulation samples include two types of neutrino interactions simulated using the GENIE [27] neutrino event generator within LArSoft [13] and the MPV generator events generated under three different generator configurations. The image preparation steps are identical to those of the training samples except for the event generation step which is unique to the generator type and configuration. This brings us to a total of six simulated samples, consisting of 120 000 events, that we can analyze with the trained network.

The neutrino samples consist of 20 000 ν_μ and 20 000 ν_e events, generated with beam flux information from the BNB [5] beam flux information. Each MPV samples includes 20 000 images of events. One MPV sample is configured to generate one proton and one electron only (1e1p). Particles are simulated with a uniform energy distribution and isotropic momentum direction distribution. The kinetic energy range is set to be 50 to 500 MeV for e^- and 50 to 300 MeV for protons. In addition, there are two more MPV samples generated: low-energy 1e1p (1e1p-LE) and low-energy 1μ1p (1μ1p-LE) where the latter is similar to 1e1p except a μ^- is generated in place of an e^-. These samples are generated in the LE range. For 1e1p-LE, the e^- has momentum distributed from 30 to 100 MeV/c. For 1μ1p-LE, the momentum of μ^- is distributed from 85 to 175 MeV/c. For both samples, the momentum of the proton is distributed from 300 to 450 MeV/c.

C. Benchmark data samples

In order to validate the network's performance on real data, we prepared two data samples for which we have a good understanding from the traditional reconstruction approaches available in LArSoft [28].

The first is a sample of Michel electron events [29], also used in our first physics result publication. This sample primarily consists of one track (stopping muon) and one shower (decay electron) and is identified using a reconstruction algorithm developed by the collaboration. The Michel electron images are simple and therefore useful to study how the network response depends on a limited amount of image features.

The second data set is a sample of charged-current (CC) ν_μ candidate interactions with one or more photons produced, primarily via π^0 decay at the interaction vertex. The CCπ^0 sample gives a different perspective than Michel electrons because it primarily consists of higher energy

showers and tracks that make the image more feature rich and complicated. Validation of the network performance on both data sets is crucial.

For the Michel electron sample we use a random subset of events identified as Michel electron events in Ref. [29]. We processed 100 data and 100 simulation events through the same waveform processing procedures applied to generate our training sample. Then we use the reconstructed decay position of the Michel electron as a constraint to crop with the CRA, which produce 512 by 512 pixel images containing both a stopping muon and a decay electron. Next we use the LAɾCV [14] toolkit to produce a pixel-level categorization of track and shower pixels through hand scanning of images by physicists. In this process, we ignored pixels that are related neither to a stopping muon nor a Michel electron. The ignored pixels are typically due to other cosmic ray muons or secondaries produced by them. This allows us to reduce the number of pixels to be labeled. The disagreement rate between the physicist labels and the U-ResNet's classification is then compared between the real data and simulated data to quantify how the network performance differs between data and simulation.

For the $CC\pi^0$ events, samples of 100 data images are identified primarily by an automated reconstruction [28]. Event selection algorithms look for a ν_μ CC interaction candidate vertex, namely a muon track with EM-showers from π^0 decay near to that vertex. Such a muon track must be either contained or associated with a proton track to reject cosmogenic backgrounds. Selected events must pass through a subsequent hand-scanning process by physicists to ensure a high purity. The reconstruction algorithm in the reconstruction chain provides an estimate of the interaction vertex position. This reconstructed vertex is used as a constraint for CRA to produce 512 by 512 pixel images. For the comparison study, we simulate events with BNB ν_μ interactions and cosmic rays. A total of 100 $CC\pi^0$ events are selected based on simulation information. The neutrino interaction vertex location from simulation information is used as a constraint for CRA to produce the same size images for simulated events. Data and simulation events are processed by an identical waveform process chain used to prepare the training sample. Finally, the pixel-level physicist labels are generated for the $CC\pi^0$ sample. The same condition is applied and the physicists labeled only pixels that are considered to be related to a neutrino interaction, ignoring pixels with cosmic ray induced energy depositions.

VI. NETWORK PERFORMANCE ON SIMULATION SAMPLES

We benchmark the performance on test simulation samples using four metrics.
  (i) ICPF mean: the average value of incorrectly classified pixel fraction per image computed over all
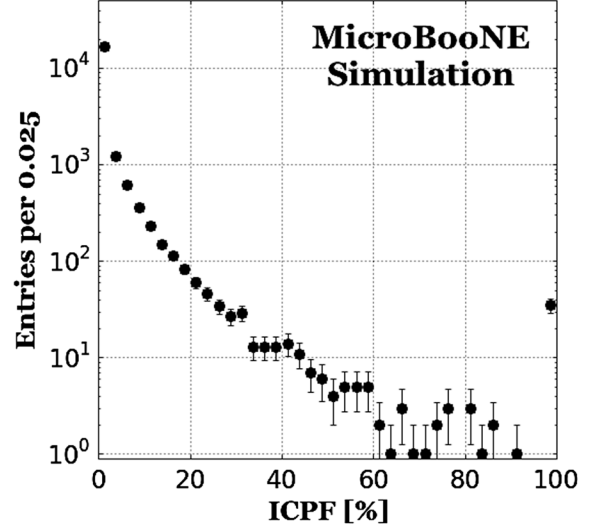

FIG. 6. The binned ICPF distribution over all images in the test set.

events in a sample. The ICPF metric is a measure that takes into account false positives and the fraction of labels for the track and shower categories.
 (ii) ICPF 90% quantile: the ICPF value below which 90% of events in a sample are present.
(iii) Shower error rate: the average value of the shower pixel error rate, defined as the fraction of incorrectly labeled shower pixels as track pixels in each image, averaged over all images in a sample.
(iv) Track error rate: the average value of the track pixel error rate, defined as the fraction of incorrectly labeled track pixels as shower pixels in each image, averaged over all images in a sample.
For all samples, the ICPF distributions are very similar. We show one example for the test sample in Fig. 6. In general, most images have very low ICPF values, well below 10% for all test samples.

The results can be found in Table I. The network is generalized to perform comparably to our test sample on

TABLE I. Values of the network performance metrics including the average of ICPF mean value, 90% quantile, the average of incorrectly classified pixel fraction for shower pixels, and the same for track pixels. The test samples described in Sec. V B. Values are shown in percentages.

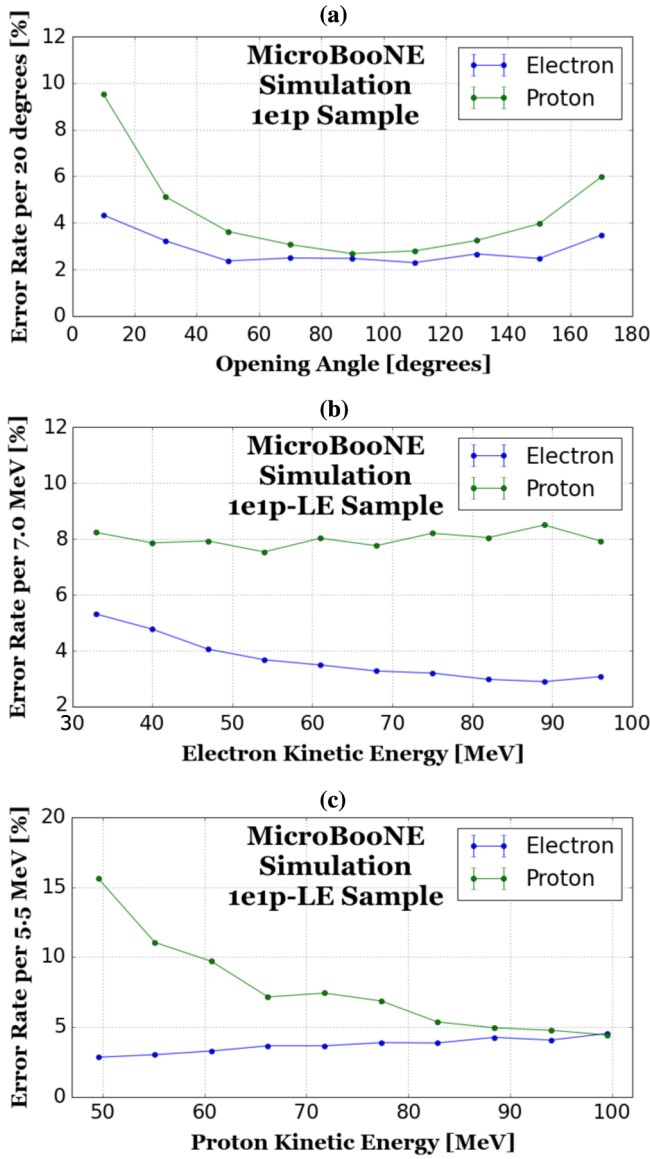| Sample	ICPF Mean	ICPF 90%	Shower	Track
Test	1.9	4.6	4.1	2.6
ν_e	6.0	13.8	7.6	13.8
ν_μ	3.9	4.5	14.2	4.3
1e1p	2.2	5.7	2.8	4.0
1μ1p-LE	2.3	2.2	6.2	2.4
1e1p-LE	3.9	11.5	3.8	8.0

FIG. 7. The ICPF error rates for U-ResNet labeling track (proton) and shower (electron) pixels for the benchmark test set are plotted against initial kinematic variables from simulation information. (a) The opening angle between two particles from the 1e1p sample. (b) The electron kinetic energy from the 1e1p-LE sample. (c) The proton kinetic energy from the 1e1p-LE sample.

into track/shower at the ICPF mean value of 3.9% and 2.3%, respectively. These are the two simplest topologies of neutrino interactions, and it is important for U-ResNet to perform well so that it can be used to distinguish the two neutrino flavors. In the 1μ1p-LE sample, despite the fact that no showers are produced in the primary neutrino interaction, challenges for the network arise from similarities between muons and electrons at very low energies and from secondary interactions like Michel electrons from muon decays.

Figure 7 shows the binned ICPF for the 1e1p and 1e1p-LE samples as a function of kinematic variables. Figure 7(a) shows the correlation with the opening angle between the two particles in 1e1p sample. We expect the ICPF value to increase when the two particles are colinear and the 2D projections overlap, making it hard to distinguish the two tracks. When they are back-to-back, the difficulty to distinguish them arises from the fact that two trajectories may appear as the trajectory of one particle. Although it is outside of the scope of this paper, some of these difficulties could be mitigated if multiple 2D projection information is incorporated.

Figures 7(b) and 7(c) show the dependence of the performance on the kinetic energy of a particle from 1e1p-LE sample. We observe that the network performs worse at lower energies. The ICPF value reaches near 15% at 50 MeV proton kinetic energy. A proton at this energy can only travel a few centimeters in LAr, which translates into 10 pixels or fewer in the collection plane image. Such a small amount of information makes the networks task difficult. A similar trend of decreasing performance can be also seen for electron kinetic energy, although the magnitude is much smaller. The critical energy above which electrons primarily produce bremsstrahlung in LAr is about 33 MeV. In the low-energy region near or below the critical energy, electrons may not show a geometrical feature of showers characterized by a cascade of radiation. Thus, the network may struggle identifying them as showers.

Overall, these kinematic distributions show the trend we expect, and set milestones to be achieved by future work on deep neural network development for LArTPC data reconstruction. A few randomly chosen example outputs of the networks are shown in the Appendix from the ν_e and ν_μ benchmark set.

VII. NETWORK PERFORMANCE WITH DETECTOR DATA AND COMPARISON TO SIMULATION

In this section we report the validation of U-ResNet on real detector data, in particular Michel electron and $CC\pi^0$ neutrino candidate events. Both data and simulation samples are processed by a physicist and contain pixel-level prediction labels. We report the comparison of the networks disagreement with a label applied by a physicist, which is considered one of the most accurate techniques for pixel

certain classes of simulated neutrino events (such as 1e1p and 1μ1p-LE) to a level that allows us to apply the technique as a part of the reconstruction chain. We do not train the network on our signal prediction—neutrino events simulated by GENIE—because this may cause the network to perform better on specific neutrino interaction models relative to others, thereby introducing a potential bias in the analysis of neutrino data. The benchmark results also demonstrate that the U-ResNet can classify pixels from the low-energy two particle topologies of 1e1p and 1μ1p

classification for LArTPC data. The details of data preparation steps are described in the previous sections.

A. Data/simulation comparison using the Michel electron sample

Table II summarizes the analysis results for the Michel electron sample. The disagreement rate between a physicist analyzer and the network prediction is below the 3% level on average for both data and simulation. Figure 8(a) shows the distribution of the pixel fractions where U-ResNet and physicists disagreed on track/shower categorization over 100 events. The calculated physicist/network labeling for data and simulation agrees within statistical uncertainty. Assuming a negligible difference in the physicists performance on data and simulation, this then implies a comparable network performance on data and simulation. Figure 8 also shows binned distributions of pixel scores for data and simulation. The track or shower label for each pixel is assigned by a physicist analyzer, and is not expected to be perfect. The score distributions show a similar trend between data and simulation. The error bars are not drawn in the score distributions since it is not trivial to derive an error for a pixel-wise score where we expect strong interpixel correlations. Finally, Table II shows that the network has a smaller ICPF when using labels generated from simulation information. The Appendix shows four randomly selected examples of Michel electron events from real data.

Further, we inspected the robustness of the network against scaling pixel values. Since there is no calibration applied at the stage of processed waveforms, we expect a difference in the signal strength between data and simulation. We run a simple differentiation algorithm to compare the signal strength between Michel data and simulation images. The algorithm inspects every pixel in an image. The algorithm finds peak pixels by comparing a given pixel with the one before and after it along the time axis to determine the one with a higher pixel value than its

TABLE II. Values of the network performance metrics for the Michel electron sample. The top row indicates the type of sample used (simulation or data), the second shows the source of a label used for analysis, and the third shows the source of a pixel prediction. The forth and the fifth rows indicate the ICPF mean value over all samples and 90% quantile, respectively. The bottom two rows show the mean of ICPF for track and shower pixels, separately. Values are given as percentages.

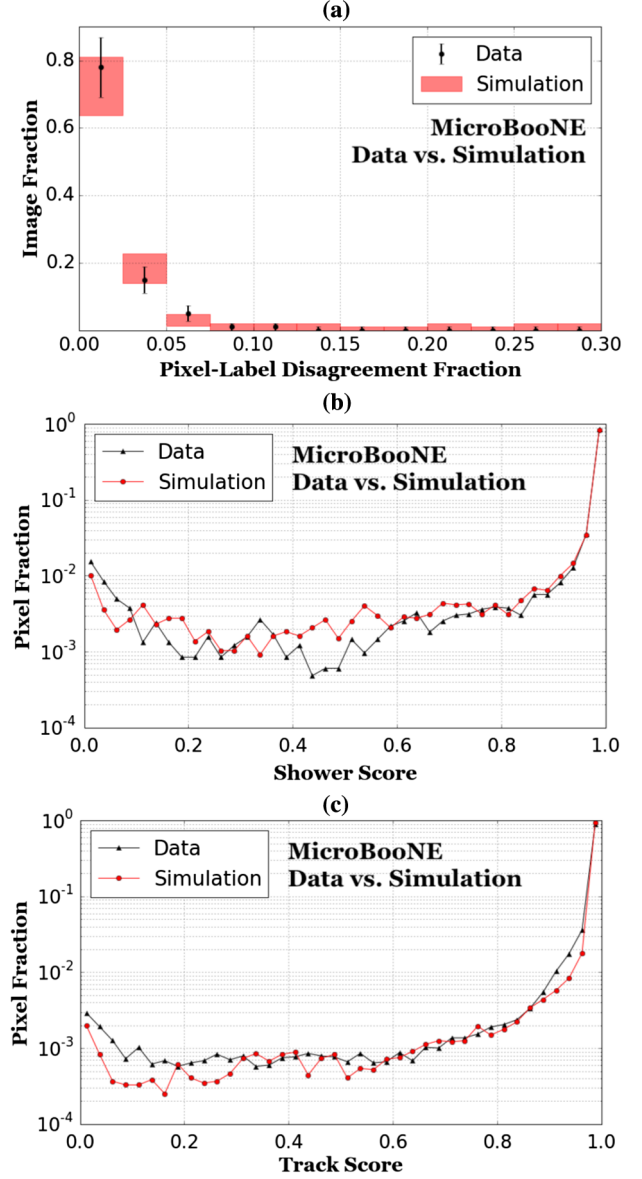| Sample	Data	Simulation	Simulation	Simulation
Label	Physicist	Physicist	Simulation	Simulation
Prediction	U-Resnet	U-ResNet	U-ResNet	Physicist
ICPF mean	1.8	2.6	2.5	2.3
ICPF 90%	3.3	4.4	4.5	3.1
Shower	6.2	5.7	4.0	3.9
Track	1.1	1.9	1.6	1.3

FIG. 8. (a) Binned distribution of ICPF for track and shower pixels where the pixel-level labels are produced by a physicist. The data and simulation distributions are area normalized and represent 100 Michel electron events. There is no event outside the shown range on the horizontal axis. (b) The normalized, binned softmax probability distributions for shower pixels on data and simulation. (c) The same as (b) for track pixels.

neighbors. This is the simplest form of a signal peak amplitude finder algorithm. The distributions for data and simulation are shown in Fig. 9, which shows a shift between the data and simulation peak positions by about 20% to 30%. For this study we scale the pixel values of data images by a constant factor and compare the performance of the network with different scaling factors. Figure 10 shows the results of this study. Although we observe that the ICPF becomes worse when we apply the scaling factor, the change is within 1% absolute when we scale pixel
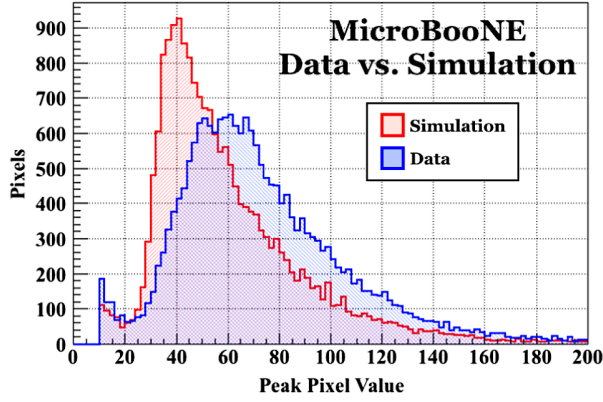
FIG. 9.   Peak pixel value distribution for Michel electron images for data and simulation using the 3-pixel differentiation algorithm described in the text. The vertical axis shows the pixel counts while the horizontal axis shows the peak pixel values.
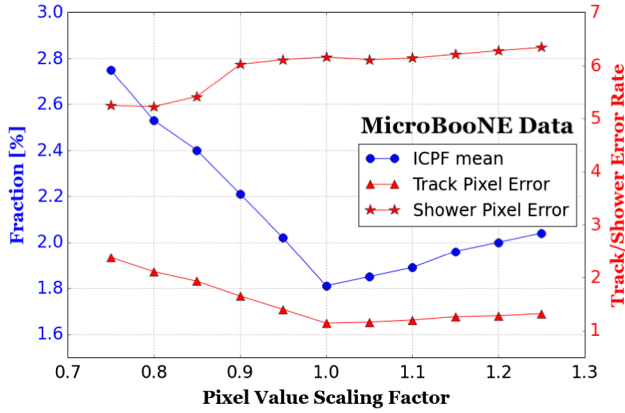

FIG. 10.   The average ICPF in percent for the Michel electron data versus pixel scaling factor is shown in blue. The pixel-fraction disagreement between physicist and network categorizations is shown in percent in red for track and shower pixels separately.

values by 25%, which is at the level of current disagreement rate between simulation and uncalibrated detector response.

B. Qualitative analysis of interpixel correlations using the Michel electron sample

We take a qualitative look at the correlation of pixel scores using the Michel electron image from one of the real data examples shown in Fig. 11. In the following sections, we focus on three regions shown in the figure. These correspond to (1) a minimum-ionizing muon track, (2) a portion of the track with high dE/dx near the muon stopping point, and (3) the low-energy Michel electron shower, respectively.

1. Minimum ionizing muon track

One possible property used to distinguish a minimum ionizing muon from a low-energy electron is the topology
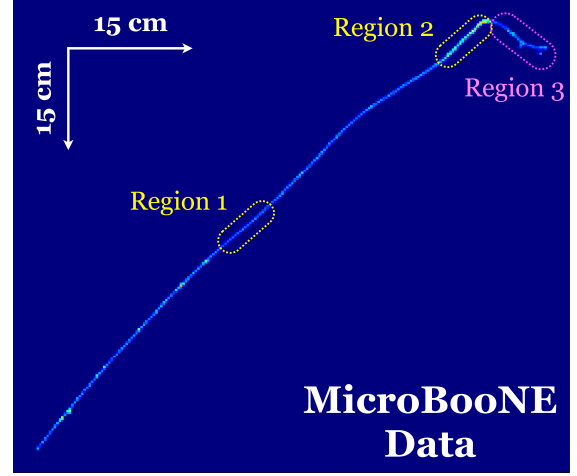

FIG. 11.   Three regions for an analysis of the interpixel correlation for a Michel in data. Region 1 contains the minimum ionizing muon trajectory. Region 2 focuses on the end of the muon trajectory where dE/dx increases. Region 3 contains a decay Michel electron.

of its trajectory. This is often a long straight line, as compared to a more "jagged" electron trajectory due to higher multiple coulomb scattering. We choose subsets of region 1 shown in Fig. 11 to test this hypothesis by masking all remaining pixels in the image to zero. Figure 12 shows the masked images and the corresponding track vs shower score distribution of non-zero (i.e., unmasked) pixels by running the U-ResNet on each image. In Figs. 12(a)–12(d), we show a series of images with increasing number of unmasked pixels to determine how the score distribution changes. When we provide only a 5-pixel long minimum ionizing track, separation is weak. The separation improves as we include more neighboring pixels, which makes the straight-track shape longer and longer. We conclude that this confirms our hypothesis that the network is focusing on the length of a straight minimum ionizing particle's trajectory.

2. Bragg peak

A stopping muon increases its energy deposition density, dE/dx, as it loses momentum and near the stopping point has the highest dE/dx called the Bragg peak. This increasing dE/dx is a useful signature to identify a stopping muon [29] and therefore make a decision that a trajectory is tracklike. In Fig. 12, we show that the network struggles with a straight, minimum ionizing tracklike trajectory of relatively few pixels. Figure 13 shows region 2 of Fig. 11, near the stopping muon's Bragg peak point, where we masked the rest of muon trajectory and the entire electron charge depositions. Track and shower score distributions are well separated at all track lengths. This is a distinct feature from Fig. 12. We therefore conclude that the network is keying on an increasing
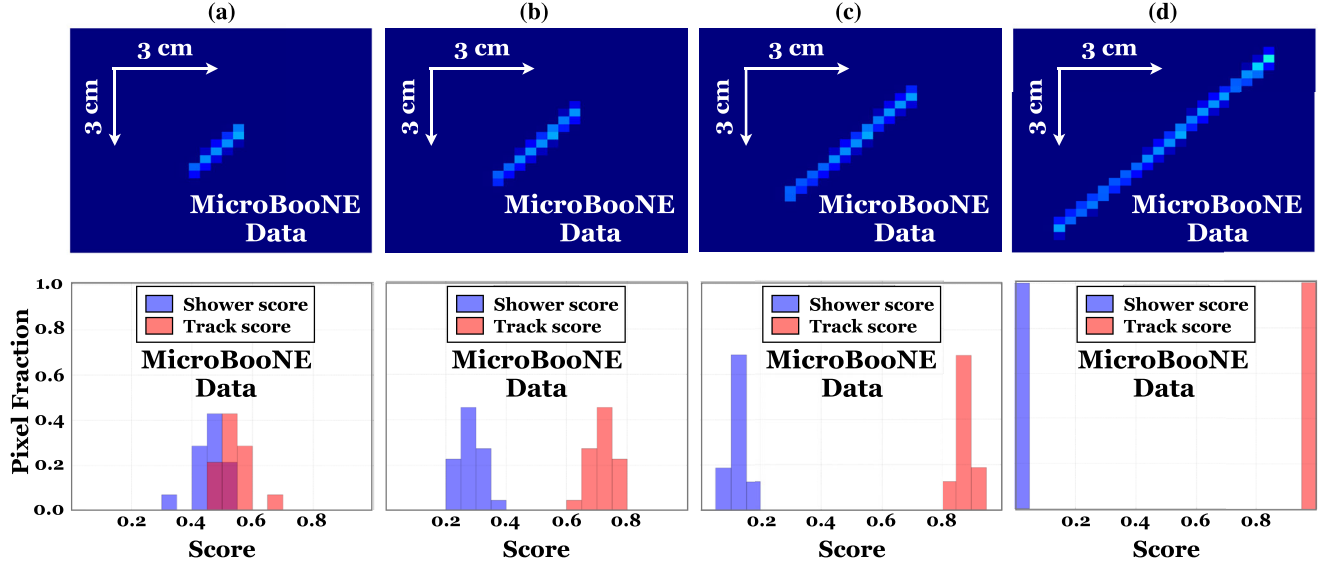
FIG. 12.   Minimum ionizing muon track in region 1 of Fig. 11 where all pixels in the image are masked except for a small portion of a muon track shown in the images above. The lower row shows normalized track vs shower score distributions for all non-zero pixels in the image.

dE/dx, or a high dE/dx, to classify a straight-line-like topology into tracklike with high confidence even if the length of such a trajectory is down to several pixels.

3. Low-energy electron shower

One key feature of an electromagnetic shower is its nonstraight line trajectory. To test this hypothesis, we take a closer look at the Michel electron charge deposition in region 3 of Fig. 11. In this event a Michel electron traveled

straight for several pixels. Then it started to scatter off of other electrons before the end of the trajectory. Because of its mass, the Michel electron is minimum ionizing for most of its trajectory. We investigate how the network's confidence varies if we separate the initial straight, minimum ionizing trajectory of a Michel electron from the remaining image.

Figure 14 shows that, where the Michel electron picture is complete, all pixels are identified strongly as a shower. We then mask the first several pixels that look
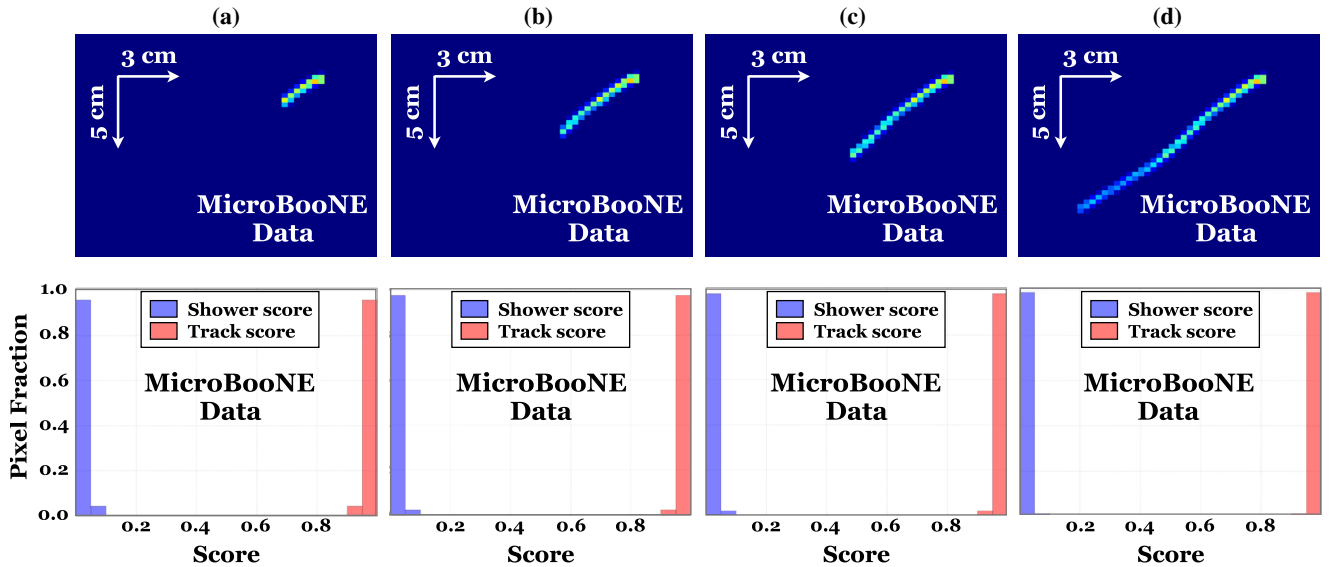

FIG. 13.   Stopping muon track in region 2 of Fig. 11 where all pixels in the image are masked except for the small portion of the muon track next to its stopping point shown in the images above. The lower row shows normalized track and shower score distributions for all nonzero pixels in the image.
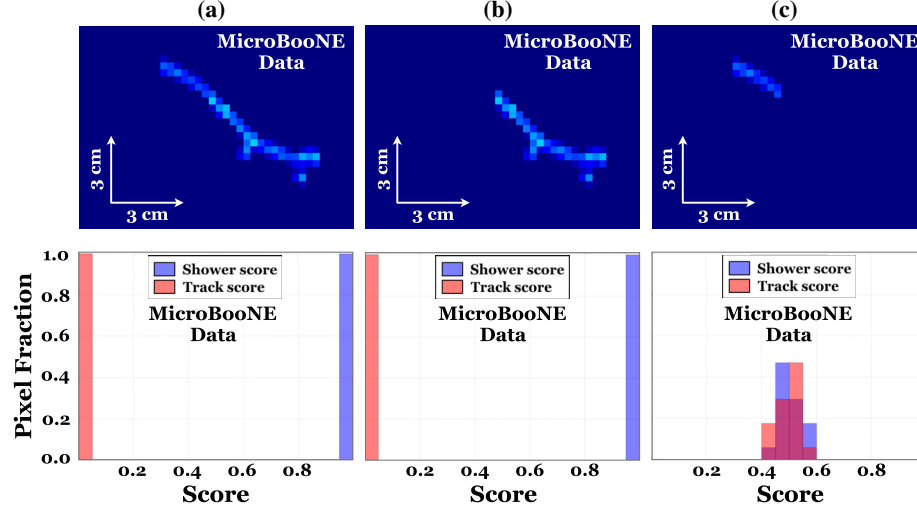
FIG. 14.   Michel electron in region 3 of Fig. 11 where all pixels in the image are masked except for a portion of an electron trajectory shown in the images above. The lower row shows normalized track and shower score distributions for all nonzero pixels in the image. (a) The entire Michel electron image is unmasked. (b) The initial portion of the Michel electron trajectory is masked. (c) Everything except the initial portion of the Michel electron trajectory is masked
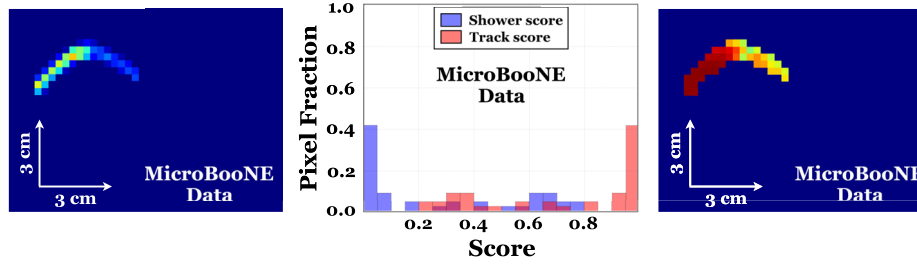

FIG. 15.   The intersection of regions 2 and 3 of Fig. 11 where all pixels in the image are masked except for a small portion of a Michel electron and the Bragg peak from a stopping muon. The middle histogram shows a normalized track and shower score distribution for all nonzero pixels in the image. The right figure shows the normalized score value of the classified pixel category.

like a track of a minimum ionizing muon [Fig. 14(b)]. The network's confidence remains very strong in this region. We also show the network's response to the first several pixels of a Michel electron [Fig. 14(c)].

TABLE III.   Values of the network performance metrics for the $CC\pi^0$ sample. The top row indicates the type of a sample used (simulation or data), the second shows the source of a label used for analysis, and the third shows the source of a pixel prediction. The forth and the fifth rows indicate the ICPF mean value over all samples and 90% quantile, respectively. The bottom two rows show the mean of ICPF for track and shower pixels, separately. Values are given as percentages.

Sample	Data	Simulation	Simulation	Simulation
Label	Physicist	Physicist	Simulation	Simulation
Prediction	U-ResNet	U-ResNet	U-ResNet	Physicist
ICPF mean	3.4	2.5	1.8	2.0
ICPF 90%	9.0	5.7	4.6	4.8
Shower	4.8	3.4	3.0	2.6
Track	2.7	2.4	2.2	2.9

The network is entirely uncertain whether this is a track or a shower in this case.

Finally, we investigate the intersection of regions 2 and 3 by adding the final pixels of the Bragg peak of the stopping muon to the first several pixels of the Michel electron, as shown in Fig. 15 We add a *heat map* which shows the score for nonzero pixels for the classified category. In the heat map we observe the dark-red region, corresponding to the score value 1, and the other region in yellow/orange color which corresponds to weaker classification scores. We also show the track and shower score distribution of all nonzero pixels. The network's confidence level remains high on classifying the Bragg peak as tracklike. Secondly, by comparing the score distribution of Fig. 15 and the score distribution in Fig. 14(c), we conclude that the beginning portion of the Michel electron now has a higher likelihood to be classified as showerlike. This suggests that the network is using the presence of the Bragg peak in the image to improve the classification of the minimum ionizing straight trajectory that starts from the end of the Bragg peak, which is otherwise ambiguous as tracklike or showerlike.

C. Data/simulation comparison using The CCπ⁰ sample

The results of running U-ResNet on the $CC\pi^0$ image samples are summarized in Table III. We find a similar trend as observed in the Michel electron sample, but with slightly higher disagreement rates. This is expected given that $CC\pi^0$ samples are complex images because of the higher number of particles and interactions involved. The top plot in Fig. 16 shows the ICPF distribution.
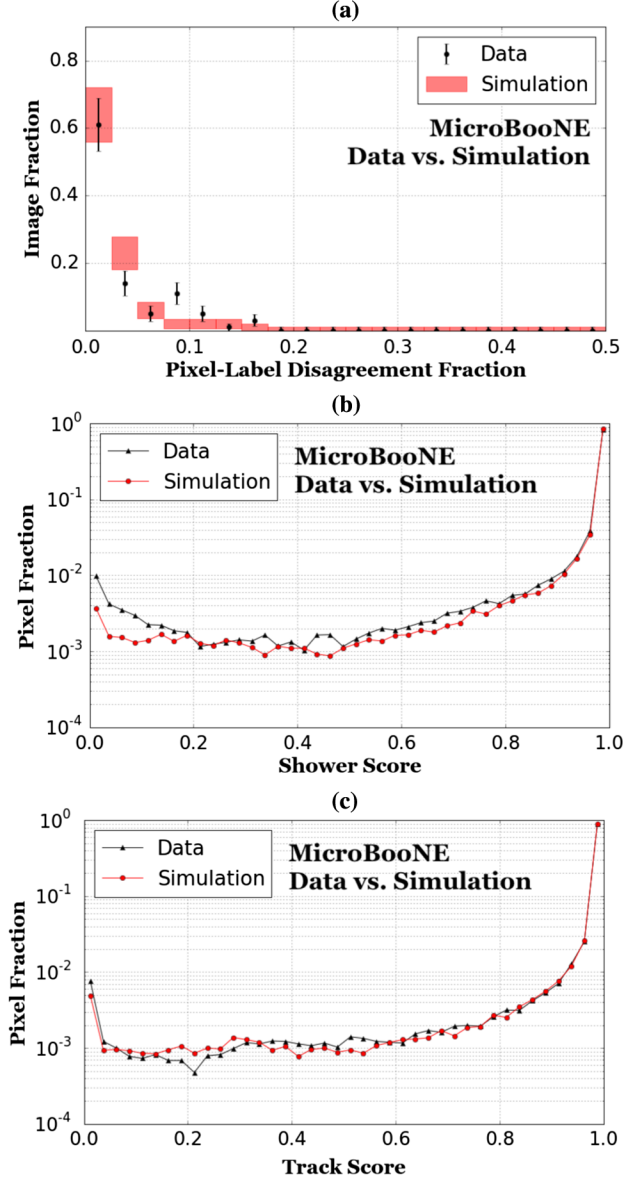

FIG. 16. (a) The binned distribution of ICPF where the pixel-level labels are produced by a physicist. The data (black) and simulation (red) distributions are area normalized, produced from 100 $CC\pi^0$ events. There is no event outside the shown range on the horizontal axis. (b) The normalized, binned softmax probability distributions for shower pixels by the network on data and simulation. (c) The same as (b) for track pixels.

As in the case of the Michel electron sample, data and simulation are in agreement within statistical fluctuations. Again assuming a negligible difference in the physicists performance on data and simulation, this implies a comparable network performance on data and simulation. In Figs. 16(b) and 16(c), we show the score distributions for the track and shower pixels labeled by a physicist. A similar trend is observed between data and simulation in both pixel categories. Four example images are shown in the Appendix with the U-ResNet output. The displayed events are visually selected by a physicist because of their particularly busy vertex activities.

Following the analysis of the Michel sample, we investigate how the scaling of pixel values in the data image affects the network performance. The result is shown in Fig. 17. We find that the ICPF values have small variation among the scaling factors applied in the study. This suggests that, although the effect is small, at the 1% level for a 25% pixel value scaling factor, mismatched signal strength in data does affect the network's response.

D. Disagreement between U-ResNet and physicist labeling for the CCπ⁰ sample

The $CC\pi^0$ events present far richer topologies than the Michel events, and we do not attempt to perform the pixel masking and the deduction exercise to learn how the network works in this sample. Instead, we study the $CC\pi^0$ data events where the disagreement between physicist and network labeling is largest. Four such events are identified and shown in Fig. 18. The four events shown are ordered by level of disagreement rates of 0.166, 0.166, 0.162, and 0.125, respectively. In the example shown on the top of the figure, the disagreement is mainly in a long tracklike trajectory originating from the interaction vertex. While a physicist analyzer decided this is a track, it could
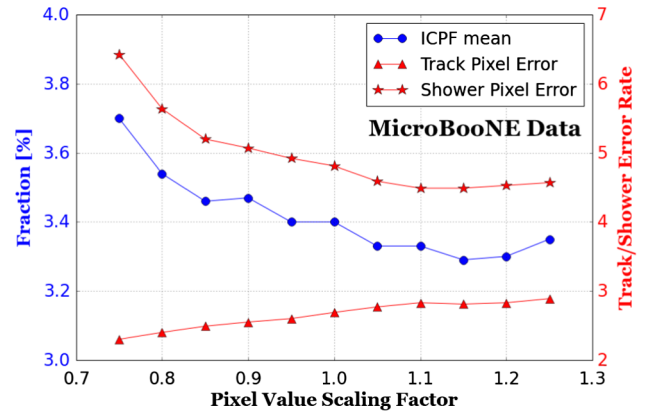

FIG. 17. The ICPF mean in percent for $CC\pi^0$ data (blue) for varying pixel scaling factor shown on the horizontal axis. A category-wise physicist-network disagreement pixel fraction in percent is shown in red for track and shower pixels separately.
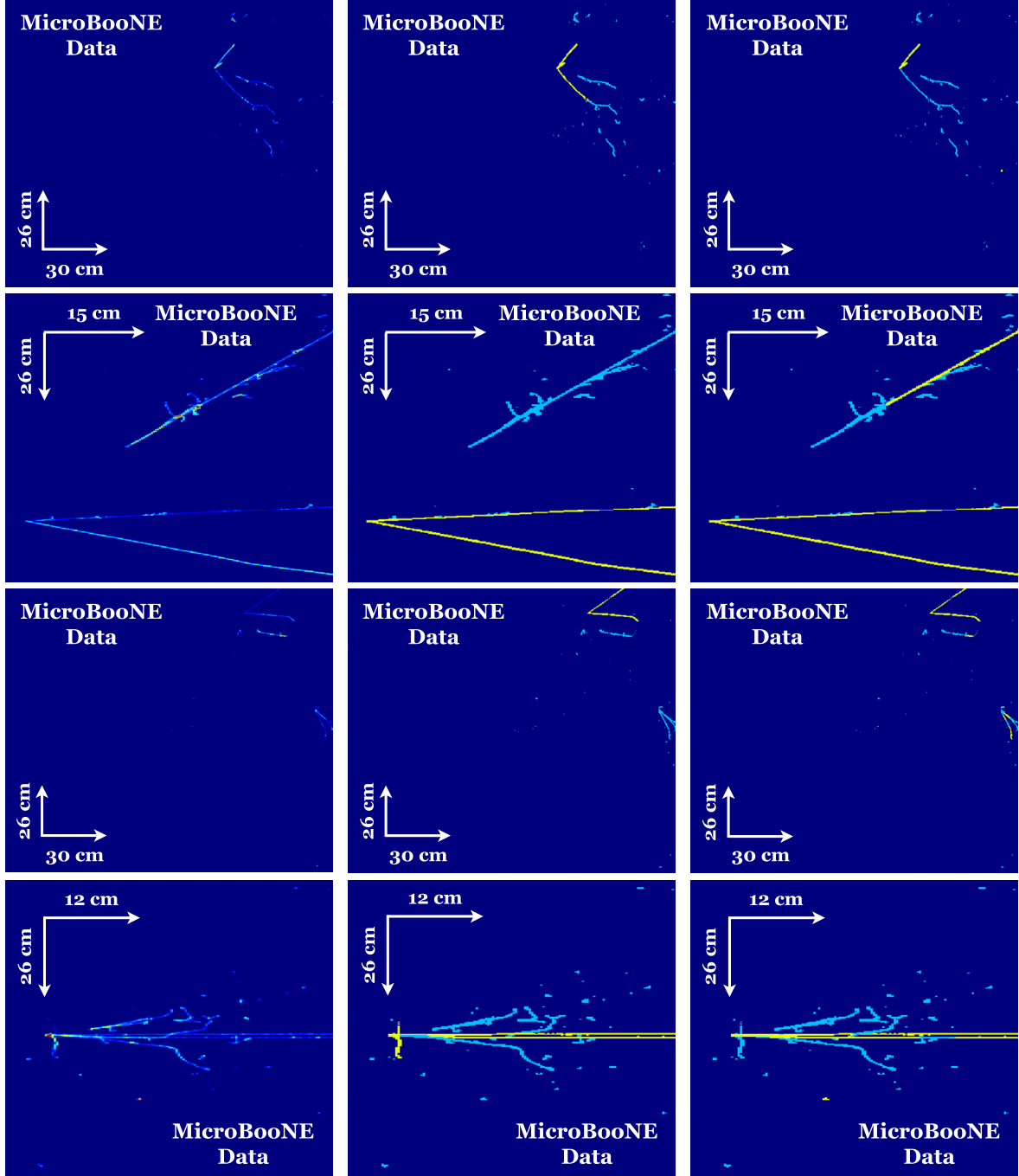
FIG. 18. Four example CCπ^0 events with highest ICPF values using physicist generated pixel labels. Left: input images to the network. Middle: track (yellow) and shower (cyan) using physicist generated labels. Right: track (yellow) and shower (cyan) labels predicted by the network.

also be a minimum ionizing electron that should be classified as a shower. The second display from the top shows the network's attempt to separate a tracklike trajectory that is present inside a high energy shower. In the third image, a large portion of particle trajectory is invisible due to unresponsive region of the detector running vertically toward the right of this image. This makes it difficult

to analyze the remaining particle trajectories where the U-ResNet mixes track and shower pixel decisions for the same trajectory. Finally, in the bottom image, the network predicts two tracklike trajectories coming from the interaction vertex while the physicist analyzer merged two tracks into one near the vertex. The region around the interaction vertex is complicated by energy deposition from

a shower, which makes it difficult to determine which decision is correct. The performance of the network for these maximal disagreement events supplements our understanding from the qualitative Michel data analysis and documents some of the ways that the network fails in categorizing pixels.

VIII. CONCLUSION

In this paper we have presented the first application of a deep semantic segmentation network, U-ResNet, to perform track/shower separation at the pixel level for LArTPC images. We explore training techniques including transfer learning and pixel-wise error weighting methods. Our software tools and algorithms to store and apply the pixel-level labeling are made available in Refs. [14,24].

U-ResNet achieved an average ICPF of 6.0% and 3.9% benchmarked with 20,000 images of ν_e and ν_μ interactions, respectively, simulated with realistic neutrino beam information. The same network achieved an average ICPF of 3.9% for 1e1p-LE events in which electrons have a uniform momentum distribution from 30 to 100 MeV/c, and protons from 300 to 450 MeV/c. The average ICPF is found to be 2.3% for 1μ1p-LE events which include protons with the same uniform momentum distribution and momentum range, and muons in a momentum range of 85 to 175 MeV/c.

We quantified and validated U-ResNet, trained purely on simulated image samples, on LArTPC images from real detector data. We calculated the fraction of incorrect pixel labeling between U-ResNet and a physicist analyzer and found an average disagreement fraction of 1.8% and 3.4% for Michel electron data and $CC\pi^0$ data, respectively. The same analysis was performed using simulation samples, and we found that the level of disagreement is consistent for data and simulation samples. This is the first time such validations have been shown on real LArTPC data. From a qualitative analysis on the Michel electron data we conclude that the network is focusing on intuitively reasonable physics features in the image. The successful application of a semantic segmentation network on LArTPC data is an important milestone toward developing a full LArTPC data reconstruction chain using a deep neural network.

APPENDIX

In this Appendix we show example event displays of simulation and data. Figure 19 shows simulated ν_e and ν_μ interactions. Figure 20 shows a stopping muon with a decay Michel electron. Figure 21 shows "busy" $CC\pi^0$ candidate events visually selected including those with a particle multiplicity greater than 4. In all of these event displays, gaps in tracks and showers are due to unresponsive wires. Overall, we observe good agreement between the simulation information and output from the network track-shower pixel labeling in diverse event types.
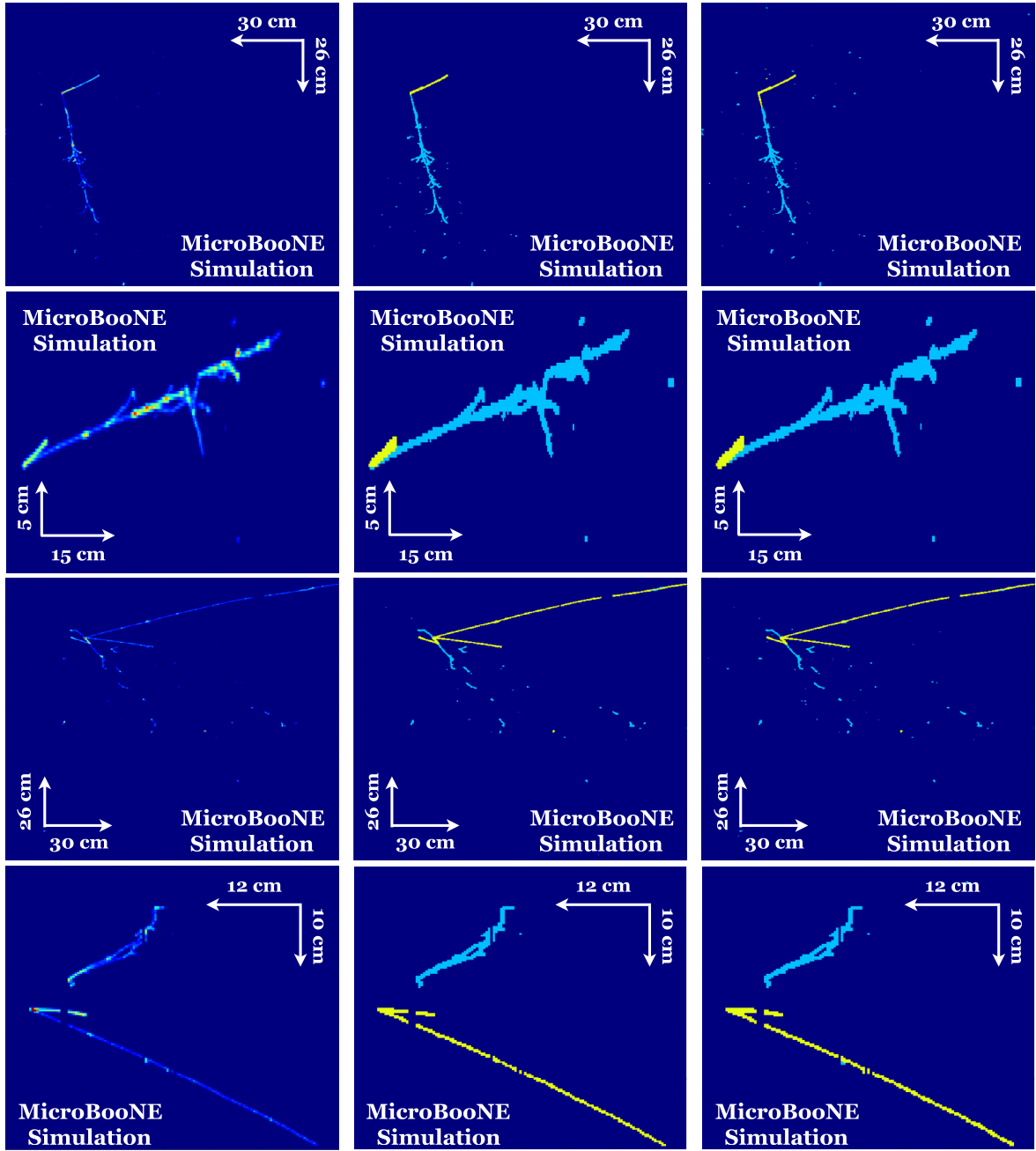
FIG. 19. Event displays of ν_e (upper two rows) and ν_μ interactions (lower two rows). The left column images are inputs to the network. The middle column shows labeled images based on simulation information. Track pixels are masked in yellow and shower pixels are in cyan. The right column shows the output of the network.
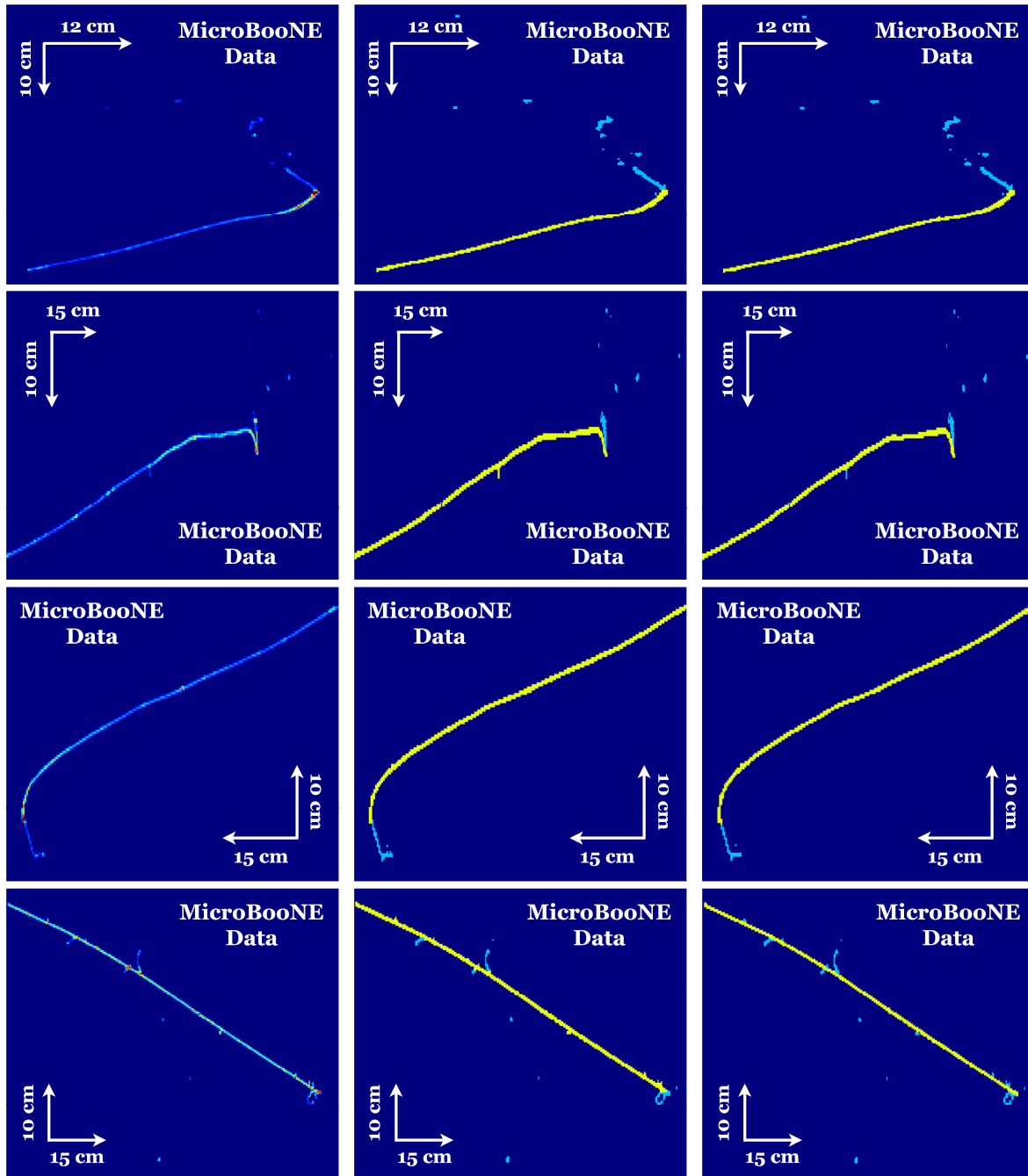
FIG. 20. Michel electron event displays from real detector data. Left: input images to the U-ResNet. Middle: track (yellow) and shower (cyan) physicist labels. Right: track (yellow) and shower (cyan) labels predicted by the network.

FIG. 21.   Neutrino event displays from CCπ^0 candidate detector data selected based on activity around the interaction vertex. Left: input images to the network. Middle: track (yellow) and shower (cyan) physicist labels. Right: track (yellow) and shower (cyan) labels predicted by the network.
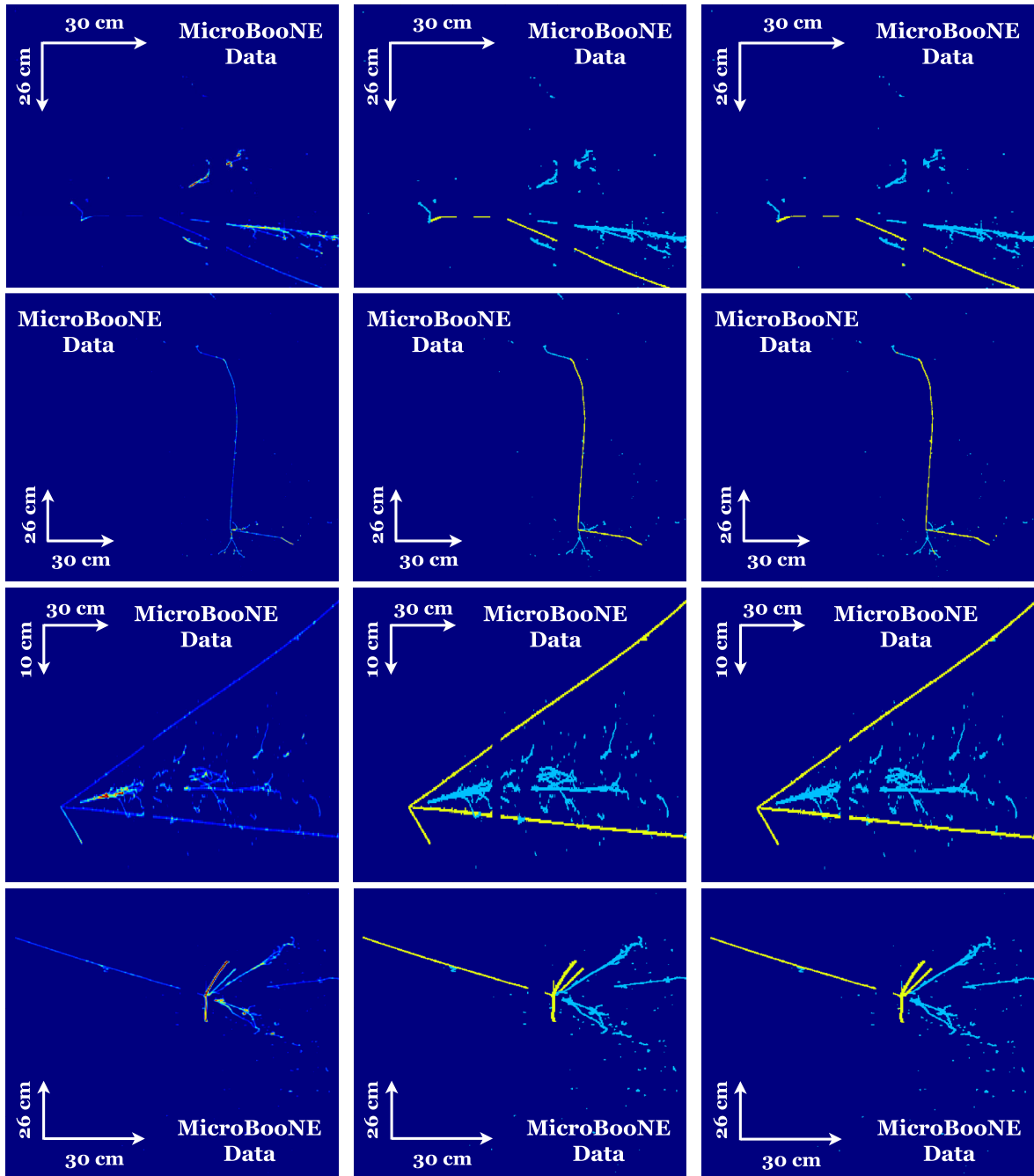
[1] M. Antonello *et al.* (MicroBooNE, LAr1-ND, and ICARUS-WA104 Collaborations), A proposal for a three detector short-baseline neutrino program in the Fermilab booster neutrino beam, arXiv:1503.01520.

[2] R. Acciarri *et al.* (DUNE Collaboration), Long-baseline neutrino facility (LBNF) and deep underground neutrino experiment (DUNE): Volume 1: The LBNF and DUNE projects, arXiv:1601.05471.

[3] R. Acciarri *et al.* (MicroBooNE Collaboration), Design and construction of the MicroBooNE detector, J. Instrum. **12,** P02017 (2017).

[4] A. A. Aguilar-Arevalo *et al.* (MiniBooNE Collaboration), Unexplained Excess of Electron-Like Events From a 1-GeV Neutrino Beam, Phys. Rev. Lett. **102,** 101802 (2009).

[5] A. A. Aguilar-Arevalo *et al.* (MiniBooNE Collaboration), The neutrino flux prediction at MiniBooNE, Phys. Rev. D **79,** 072002 (2009).

[6] R. Acciarri *et al.* (MicroBooNE Collaboration), Noise characterization and filtering in the MicroBooNE liquid argon TPC, J. Instrum. **12,** P08003 (2017).

[7] R. Acciarri *et al.* (MicroBooNE Collaboration), Convolutional neural networks applied to neutrino events in a liquid argon time projection chamber, J. Instrum. **12,** P03011 (2017).

[8] A. Aurisano, A. Radovic, D. Rocco, A. Himmel, M. D. Messier, E. Niner, G. Pawloski, F. Psihas, A. Sousa, and P. Vahle, A convolutional neural network neutrino event classifier, J. Instrum. **11,** P09001 (2016).

[9] E. Racah, S. Ko, P. Sadowski, W. Bhimji, C. Tull, S.-Y. Oh, P. Baldi, and M. Prabhat, Revealing fundamental physics from the Daya Bay neutrino experiment using deep neural networks, in *Proceedings of the IEEE International Conference on Machine Learning and Applications (ICMLA)* (IEEE, Anaheim, 2016).

[10] J. Renner *et al.* (NEXT Collaboration), Background rejection in NEXT using deep neural networks, J. Instrum. **12,** T01004 (2017).

[11] A. Radovic, M. Williams, D. Rousseau, M. Kagan, D. Bonacorsi, A. Himmel, A. Aurisano, K. Terao, and T. Wongjirad, Machine learning at the energy and intensity frontiers of particle physics, Nature (London) **560,** 41 (2018).

[12] G. N. Perdue *et al.* (MINERvA Collaboration), Reducing model bias in a deep learning classifier using domain adversarial neural networks in the MINERvA experiment, J. Instrum. **13,** P11020 (2018).

[13] LArSoft release redmine 06.26.01, https://cdcvs.fnal.gov/redmine/projects/larsoft/wiki/ReleaseNotes062601.

[14] V. Genty, K. Terao, and T. Wongjirad, LArCV: LArTPC image processing/analysis framework for deep learning https://www.github.com/LArbys/LArCV.

[15] O. Ronneberger, P. Fischer, and T. Brox, U-net: Convolutional networks for biomedical image segmentation, Med. Image Comput. Comput. Assist. Interv. **9351,** 234 (2015).

[16] K. He, X. Zhang, S. Ren, and J. Sun, Deep residual learning for image recognition, in *Proceedings of the IEEE Conference on Computer Vision and Pattern Recognition (CVPR), 2016* (IEEE, Las Vegas, 2016), p. 770.

[17] M. Drozdzal, E. Vorontsov, G. Chartrand, S. Kadoury, and C. Pal, The importance of skip connections in biomedical image segmentation, in *Deep Learning and Data Labeling for Medical Applications. DLMIA 2016, LABELS 2016*, edited by G. Carneiro *et al.*, Lecture Notes in Computer Science, Vol. 10008 (Springer, Cham, 2016), pp. 179–187.

[18] Z. Zhang, Q. Liu, and Y. Wang, Road extraction by deep residual U-net, IEEE Geosci. Remote Sens. Lett. **15,** 749 (2018).

[19] S. Ioffe and C. Szegedy, Batch normalization: Accelerating deep network training by reducing internal covariate shift, arXiv:1502.03167.

[20] S. Agostinelli *et al.*, GEANT4: A simulation toolkit, Nucl. Instrum. Methods Phys. Res., Sect. A **506,** 250 (2003).

[21] T. Tieleman and G. Hinton, Lecture 6.5-rmsprop: Divide the gradient by a running average of its recent magnitude (unpublished).

[22] Y. Jia *et al.*, Caffe: Convolutional architecture for fast feature embedding, arXiv:1408.5093.

[23] NVIDIA GeForce Titan X GPU Card specification, http://www.geforce.com/hardware/desktop-gpus/geforce-gtx-titan-x/specifications.

[24] uboonecode release redmine 06.26.01.13, https://cdcvs.fnal.gov/redmine/projects/uboonecode.

[25] C. Adams *et al.* (MicroBooNE Collaboration), Ionization electron signal processing in single phase LArTPCs I. Algorithm description and quantitative evaluation with MicroBooNE simulation, J. Instrum. **13,** P07006 (2018).

[26] C. Adams *et al.* (MicroBooNE Collaboration), Ionization electron signal processing in single phase LArTPCs II. Data/Simulation comparison and performance in MicroBooNE, J. Instrum. **13,** P07007 (2018).

[27] C. Andreopoulos *et al.*, The GENIE neutrino Monte Carlo generator, Nucl. Instrum. Methods Phys. Res., Sect. A **614,** 87 (2010).

[28] R. Acciarri *et al.* (MicroBooNE Collaboration), The Pandora multi-algorithm approach to automated pattern recognition of cosmic-ray muon and neutrino events in the MicroBooNE detector, Eur. Phys. J. C **78,** 82 (2018).

[29] R. Acciarri *et al.* (MicroBooNE Collaboration), Michel electron reconstruction using cosmic-ray data from the MicroBooNE LArTPC, J. Instrum. **12,** P09014 (2017).